Substantial Oxygen Loss and Chemical Expansion in Lithium-Rich Layered Oxides at Moderate Delithiation

Peter M. Csernica[1], Kit McColl[2], Grace M. Busse[1], Kipil Lim[1], Diego F. Rivera[1], David A. Shapiro[3], M. Saiful Islam[4*], and William C. Chueh[1,5*]

[1]*Department of Materials Science and Engineering, Stanford University, Stanford, CA 94305, USA.*

[2]*Department of Chemistry, University of Bath, Bath BA2 7AY, UK*

[3]*Advanced Light Source, Lawrence Berkeley National Laboratory, Berkeley, CA 94720, USA*

[4]*Department of Materials, University of Oxford, Oxford OX1 3PH, UK*

[5]*Stanford Institute for Materials and Energy Sciences, SLAC National Accelerator Laboratory, Menlo Park, CA 94025, USA.*

* Corresponding authors: saiful.islam@materials.ox.ac.uk, wchueh@stanford.edu

Abstract

Delithiation of layered oxide electrodes triggers irreversible oxygen loss, one of the primary degradation modes in lithium-ion batteries. However, the delithiation-dependent mechanisms of oxygen loss remain poorly understood. Here, we investigate the oxygen nonstoichiometry in Li- and Mn-rich $Li_{1.18-x}Ni_{0.21}Mn_{0.53}Co_{0.08}O_{2-\delta}$ electrodes as a function of Li content by utilizing cycling protocols with long open-circuit voltage steps at varying states of charge. Surprisingly, we observe significant oxygen loss even at moderate delithiation, corresponding to 2.5, 4.0 and 7.6 mL O_2 g^{-1} after resting at 135, 200, and 265 mAh g^{-1} (relative to the pristine material) for 100 h. Our observations suggest an intrinsic oxygen instability consistent with predictions of high equilibrium oxygen activity at intermediate potentials. From a mechanistic viewpoint, we show that cation disorder greatly lowers the oxygen vacancy formation energy by decreasing the coordination number of transition metals to certain oxygen ions. In addition, we observe a large chemical expansion coefficient with respect to oxygen nonstoichiometry, which is about three times greater than those of classical oxygen-deficient materials such as fluorite and perovskite oxides. Our work challenges the conventional wisdom

that deep delithiation is a necessary condition for oxygen loss in layered oxide electrodes and highlights the importance of calendar aging for investigating oxygen stability.

Introduction

Irreversible oxygen loss is a well-known challenge in Li- and Mn-rich (LMR) layered oxide materials, which are promising positive electrodes for lithium-ion batteries[1]. This phenomenon, written in Kröger-Vink notation in Eq. (1), involves transition metal (TM) reduction, oxygen vacancy ($V_O^{\cdot\cdot}$) formation, and the irreversible loss of oxygen from the crystalline lattice:

$$O_O^{\times} + 2TM_{TM}^{\times} \rightarrow V_O^{\cdot\cdot} + 2TM_{TM}^{\prime} + \frac{1}{2}O_2(g) \qquad (1)$$

In general terms, we use O_2 in Eq. (1) to represent any oxygen lost from the crystalline lattice that is unable to return to its original O^{2-} state. Most intuitively, it would include molecular gaseous oxygen which has been observed directly during the first delithiation of LMR electrodes[2–5]. Additionally, the O_2 term also includes either oxygen which reacts with the electrolyte or which dimerizes during cycling[6–10] and is unable to return to its original O^{2-} state. Regardless of the exact identity of the O_2 term, the irreversible loss of oxygen from the lattice will modify the electrochemically-active redox couples[11–16], lower the cell voltage[11], and contribute to cation disordering within the crystalline lattice through vacancy (Schottky) defect pairs[11,12,17]. We note that Eq. (1) considers the fully lithiated (i.e. discharged) material, and thus a fully lithiated material which has experienced oxygen loss over cycling will exhibit a reduced TM oxidation state compared to that of the pristine material. At intermediate points within the charge/discharge cycle, the charge compensation for lost oxygen will vary. Particularly at surfaces, oxygen vacancies may be eliminated from the lattice through densification[11,18,19], a process which also results in TM reduction.

Oxygen loss from LMR materials has been observed both during initial delithiation[2–5] and after one or more complete electrochemical cycles[11–16]. In both of these situations, the effect of Li content on oxygen loss has not been determined. Because gas evolution experiments typically do not detect $O_2(g)$ until charging to ~ 225 mAh g^{-1} (relative to the pristine material)

[2,3,4,20,21], lattice oxygen in LMR materials is considered to be relatively stable at lower states-of-charge (SoCs). However, seminal work[22,23] from Godshall, Raistrick, and Huggins in 1984 on the relationship between oxygen partial pressure (i.e. oxygen activity) and voltage vs. Li/Li^+ (i.e., lithium activity) implies that oxygen would be thermodynamically unstable throughout the entire charge-discharge cycle of LMR materials. It is therefore crucial to develop a more complete understanding of the relationship between Li content and oxygen loss.

With regard to kinetics, low Li contents are expected to promote oxygen diffusion. Temperature-programmed experiments demonstrate that oxygen loss occurs at the lowest temperatures (between 150 – 300 ºC) when the Li^+ content is at a minimum[12,24]. Conversely, fully lithiated LMR materials take > 50 h at 600 ºC to equilibrate their oxygen content with that of their surroundings[25,26], implying a much slower oxygen diffusivity at high Li contents. Mechanistically, this may be due to the formation of oxidized oxygen species at low Li contents, which is believed to be a prerequisite for oxygen mobility. One possibility is that molecular O_2, a form of oxidized oxygen, is transported through a percolating network of nanovoids[27]. Other forms of oxidized oxygen, such as O^- or O_2^{2-}, may also contribute to transport[28–30]. Nonetheless, beyond this qualitative trend, the relationship between Li content and oxygen loss is not well-established for LMR materials.

In this work, we systematically investigate irreversible oxygen loss in $Li_{1.18-x}Mn_{0.53}Ni_{0.21}Co_{0.08}O_{2-\delta}$ (LMR-NMC) as a function of Li content. We perform X-ray absorption spectroscopy (XAS) on electrodes subjected to long open-circuit voltage (OCV) resting steps at different SoCs. These experiments are conducted during the first cycle of LMR-NMC to limit both the microstructure change and cation disordering[11,31–33]. While irreversible oxygen loss has been well-documented for fully charged electrodes[2], surprisingly, we show that oxygen loss in the absence of cycling is extensive even at SoCs as low as charging the pristine material to 135 mAh g^{-1}. Quantitatively, we observed an oxygen loss equivalent to 2.5 ± 0.2, 4.0 ± 0.4, and 7.6 ± 0.6 mL O_2 (25 ºC and 1 atm) per gram of LMR-NMC after resting at 135, 200, and 265 mAh g^{-1} for 100 h, respectively. We further show an unusually large lattice chemical expansion in the fully discharged state (0.17%, 0.64%, and 1.4% after resting at 135, 200, and 265 mAh g^{-1} for 100 h, respectively) that is significant compared to the lattice contraction due to delithiation. The large chemical expansion observed, which we attribute to

oxygen nonstoichiometry, establishes a direct link between oxygen loss and mechanical degradation (e.g. particle cracking). Density-functional theory (DFT) calculations show that oxygen vacancies prefer atomic sites with a large number of non-transition metal (i.e. Li) neighbors, indicating that disordered oxides, even at full lithiation, are more unstable with respect to oxygen loss. In LMR-NMC, the extent of disorder increases over cycling[11], increasing the concentration of possible sites for oxygen vacancies. This work highlights the significant challenge of preventing oxygen loss in LMR materials, particularly when they are calendar-aged at moderate to high SoCs, and reveals an unusually large chemical expansion coefficient that exacerbates microstructural degradation.

Oxygen Loss During OCV Rests

Oxygen loss is typically observed after full electrochemical cycles[11,13,15]. Here, to isolate the effect of Li content on oxygen loss in LMR-NMC, as-fabricated electrodes were delithiated to different Li contents at 13.5 mA g^{-1} (~C/20). Upon reaching the targeted Li content, we rest the electrodes at OCV for either 1 min or 100 h. Subsequently, these cells were discharged at 13.5 mA g^{-1} to 2.5 V vs. Li/Li^+ and held at that voltage for ~ 16 h to relithiate (Fig. 1a). Finally, X-ray absorption spectroscopy, microscopy, and diffraction were taken in the discharged state. For each calendar aging experiment, the electrodes never experienced delithiation beyond the resting SoC. We note that the LMR-NMC material used here has excellent low-rate capacity retention[11] (> 95% over 500 cycles).

The Mn oxidation states of LMR-NMC electrodes determined through K-edge XAS are shown in Fig. 1b (see Fig. 2 for L-edge XAS). First, as a baseline, for LMR-NMC exposed to electrolyte for > 300 h without cycling, only a small amount of TM reduction is observed (Mn^{4+} to $Mn^{3.98+}$). This is may be due to the formation of a surface reconstruction layer, which has been shown to form with electrolyte exposure even in the absence of cycling[34]. Second, the Mn oxidation state of the cycled samples decreases substantially (to as low as $Mn^{3.81+}$), with electrodes charged to higher SoCs exhibiting lower Mn oxidation states. Finally, the extent of Mn reduction increases systematically with open-circuit resting time, even for samples which are only charged to moderate SoCs (e.g. 135 – 200 mAh g^{-1}).

A reduction in the TM oxidation state (evaluated with the integral method[35]) is an indicator of oxygen loss on the basis of electroneutrality (see Eq. (1)), calculated here in the same way as in our previous work[11]. We note that, while the Li content of the cycled material is slightly lower than that of the pristine material (Supplementary Table 1), incomplete relithiation, which may be due to densification on the particle surface[11,18], does not explain the observed TM reduction. Rather, because Li loss is charge balanced with TM oxidation, the fact that there is incomplete relithiation indicates that we are slightly underestimating the actual amount of oxygen loss (Supplementary Note 1).

The calculated oxygen loss quantities, summarized in Supplementary Table 2, are surprising, as gas evolution experiments typically detect oxygen gas only at the very end of charging (at SOCs > 225 mAh g^{-1})[2,3,4,20,21]. In contrast, for example, our results show that an electrode charged only to 200 mAh g^{-1} and rested for 100 h loses 1.4 at. % of O (Supplementary Table 2). Even for electrodes charged to 135 mAh g^{-1}, immediately prior to the high-voltage plateau (Fig. 1a), we observe up to 0.9 at. % oxygen loss (Supplementary Table 2). The observation of oxygen loss after charging to 135 mAh g^{-1}, together with previous observations of negligible oxidized oxygen upon charging to this SoC (without calendar aging)[36], calls into question the hypothesis that oxidized oxygen is necessary for oxygen transport in LMR materials. We note that the discrepancy between gas evolution measurements and implied oxygen loss from XAS experiments may be due to the fact that the former generally have difficulty detecting low rates of oxygen loss occurring over extended periods of time. One reason for this is that oxygen may react with other species in the battery before escaping as a gas[3].

To understand the spatial distribution of Mn reduction, we turn to scanning transmission X-ray microscopy (STXM), performed at the Advanced Light Source (ALS)[37]. Here, we map the nanoscale Mn oxidation state utilizing the Mn L_3-edge[11]. Figure 2a–c shows STXM images of the Mn oxidation state for the pristine sample as well as those of samples charged to 200 and 265 mAh g^{-1}, rested for 100 h at OCV, and discharged to 2.5 V vs. Li/Li^+ (with a ~16 hr voltage hold). While Mn in the pristine material is in the 4+ state, we observe a significant Mn reduction in the discharged electrodes which had been charged to 200 or 265 mAh g^{-1} (Fig. 2d). This finding corroborates the results shown in Figure 1b, which were taken at the Mn K-edge, providing unambiguous evidence of Mn reduction in the cycled electrodes. Interestingly, Fig. 2e

reveals that a significant amount of Mn reduction is observed even in thicker regions of the electrode particles shown here. This observation directly reveals that bulk LMR-NMC is oxygen deficient, even for electrodes charged to just 200 mAh g^{-1}.

Single-Phase Lattice Expansion

Similar to our previous report on LMR-NMC during cycling-induced aging[11], the electrodes maintained their native layered structure following calendar aging (Fig. 3a,b and Supplementary Fig. 1). However, following the initial cycle, we observed a lattice expansion (compared to the pristine material) along both the a and c axis (Fig. 3a,b and Supplementary Fig. 2). The lattice volume expansion is significant, reaching 1.4% for the sample which was rested for 100 h at 265 mAh g^{-1}. The single-cycle lattice expansion was larger for electrodes charged to and rested at a higher SoC (Fig. 3c). Lattice expansion in LMR materials is indicative of oxygen vacancies, as the formation of oxygen vacancies reduces TM species and results in longer M–O bonds[11]. Indeed, combining the XAS results with the lattice volume measurements (Supplementary Tables 2 and 3) reveals that the lattice volume is essentially linear with the amount of oxygen loss (Fig. 3d) and with the Mn oxidation state (Supplementary Fig. 3). We note that the c lattice parameter is no longer linear with oxygen vacancy concentration after ~ 4 at. % O has been removed from the lattice (Supplementary Fig. 2). We acknowledge that cation disordering concomitant with oxygen loss may also contribute to the evolution of the lattice constants.

Importantly, because the lattice volume in LMR materials is known to contract at the beginning of charge with delithiation[38], the lattice expansion observed here cannot be attributed solely to incomplete re-lithiation on discharge. Consistent with our findings, previous work[38] also shows that the lattice parameters of the lithiated state are highly sensitive to the cycling history. Only electrodes which are first charged to a high SoC experience lattice expansion in the lithiated state relative to the pristine material.

Lattice expansion due to oxygen nonstoichiometry is a well-known phenomenon in many oxides, with ceria and perovskites (such as $LaTMO_3$) being among the most familiar examples[39–42]. Quantitatively, the relationship between the lattice volume and oxygen nonstoichiometry is quantified via the chemical expansion coefficient[42], α_c, which relates the compositional

eigenstrain, ε, to the fractional concentration of oxygen vacancies, $[V_O^{\cdot\cdot}]$: $\varepsilon = \alpha_c[V_O^{\cdot\cdot}]$. Note that $[V_O^{\cdot\cdot}]$ is normalized to the entire oxygen sublattice[42]. Fitting to the linear trend between lattice volume and amount of oxygen loss in Fig. 3d, we obtain an unusually large chemical expansion coefficient, α_c, of 0.68. This value is quite striking considering that most perovskites[42] have α_c values determined with respect to $[V_O^{\cdot\cdot}]$ near 0.1. Even ceria[42], a material well-known for its lattice expansion induced by the presence of oxygen vacancies, has a α_c value calculated with respect to $[V_O^{\cdot\cdot}]$ of ~ 0.2. The large α_c for LMR-NMC can result in a greater than 4% lattice expansion over cycling[11], which likely contributes to material cracking, thereby decreasing the oxygen diffusion length and accelerating degradation.

Energetics of oxygen vacancy formation

To better understand where oxygen vacancies prefer to form crystallographically in LMR-NMC, DFT calculations were performed to investigate the energetics of oxygen vacancies at different sites in both the pristine structure and in the disordered structure after cycling. To represent LMR-NMC, which exhibits disorder and nanodomains[43], we used a model representative Li-rich Co-free composition of $Li_{1.16}Mn_{0.67}Ni_{0.16}O_2$. For the pristine structure, we first determined the distribution of different local oxygen coordination environments using cluster expansion and Monte Carlo simulations (Methods). Figure 4a (and Supplementary Fig. 4) shows the distribution of O environments in the pristine material, which indicates that all O ions are coordinated to either two or three TM (*i.e.*, Mn, Ni) ions: 50% are O–Li_3TM_3 and 50% are O–Li_4TM_2.

To represent the structure after cycling, which introduces crystallographic site disorder into the structure due to TM ion migration[36] (Supplementary Table 3), we used a special quasirandom structure (SQS), which approximates a randomly disordered configuration[44]. The cycled electrode model (Figure 4b) contains a distribution of oxygen coordination environments; some O atoms have zero or one TM neighbor (O–Li_6, O–Li_5TM) whilst some have four or five TM neighbors (O–Li_2TM_4, O–$LiTM_5$). The SQS model contains no O sites with six TM neighbors (O–TM_6), which, statistically, have a low probability of appearing because the material has a high Li to TM ratio.

To understand the preferred location of oxygen vacancies in the structure, the formation energies of oxygen vacancies ($\Delta E(O_{vac})$) at different sites (of the defect reaction in Eq. 1) were calculated according to the following equation:

$$\Delta E(O_{vac}) = \left[E(V_O^{\cdot\cdot} + 2TM'_{TM}) + \frac{1}{2}E\left(O_{2(g)}\right)\right] - E(O_O^{\times} + 2TM_{TM}^{\times}) \qquad (2)$$

Here, $E(O_O^{\times} + 2TM_{TM}^{\times})$ is the energy of a structural model with all the O sites occupied, $E(V_O^{\cdot\cdot} + 2TM'_{TM})$ is the energy of the same structure but with a single oxygen vacancy charge-compensated by the reduction of two transition metal (TM) ions, and $E\left(O_{2(g)}\right)$ is the energy of a gaseous oxygen molecule.

Figure 4a,b shows the values of $\Delta E(O_{vac})$ at different O sites in the pristine and cycled structure, plotted according to the coordination of the O site to TM neighbors. Sites in the pristine structure with O–Li_3TM_3 and O–Li_4TM_2 coordination have high positive oxygen vacancy formation energies between 2.5 eV and 5.0 eV. Such high formation energies for these sites indicate that O vacancies will not be prevalent in the pristine electrode, consistent with previous observations[26]. O–Li_2TM_4 and O–$LiTM_5$ sites in the cycled electrode also exhibit high $\Delta E(O_{vac})$.

Conversely, sites with O–Li_5TM and O–Li_6 coordination, which appear only after cation disordering, have substantially lower oxygen vacancy formation energies. O–Li_5TM sites have $\Delta E(O_{vac})$ values predominantly below 2 eV. Interestingly, O–Li_6 sites have negative $\Delta E(O_{vac})$, indicating that it is thermodynamically favorable for oxygen vacancies to spontaneously form at these oxygen sites. As a general rule, oxygen vacancies prefer sites that have a large number of Li (i.e. non-TM) neighbors. Importantly, because these calculations were carried out on the fully lithiated material, our results imply that disordered oxides can be unstable to oxygen loss even in the fully lithiated/reduced state. Furthermore, we emphasize that $\Delta E(O_{vac})$ is expected to be more negative (i.e. oxygen vacancy formation will be more favorable) once the material has been delithiated[28,45] (see Supplementary Note 2).

To better understand the origin of the unusually large chemical expansion coefficient observed experimentally, we also performed DFT calculations in which we increased the number of oxygen vacancies in the SQS cell up to 6.25% oxygen deficiency. Supplementary Fig. 5 shows

the unit cell volume as a function of the number of oxygen vacancies. As found experimentally, there is an expansion in the unit cell volume as the number of oxygen vacancies increases, with a large α_c of around 0.22. This relatively large α_c is qualitatively consistent with the large experimental chemical expansion coefficient. With that said, it is still lower than our experimental α_c value of 0.68. This discrepancy may be due to various factors including compositional differences and additional structural changes (e.g. dislocations[46]) associated with oxygen loss that occur over cycling and are not fully captured in our DFT simulations.

Open-Circuit Voltage Relaxation

Previous studies have found that oxygen loss and the concomitant TM reduction lowers the discharge voltage of LMR materials over cycling[11,12]. Consistent with such work, Fig. 5 shows that there is a notable decrease (up to ~ 240 mV) in the voltage of LMR–NMC during the open-circuit resting period[2] of 100 hours. The voltage drop during open-circuit trends systematically with SoC, and therefore with oxygen loss (Fig. 1b). Interestingly, the discharge curves following the rest periods also occur at lower voltages (Supplementary Fig. 6) than those of electrodes which do not experience a rest period. We note that the additional coulombic inefficiency during calendar aging is nearly constant as a function of resting capacity (Supplementary Fig. 7). Therefore, it is unlikely that the results in Fig. 5b can be explained solely by self-discharge of the cells during resting. While the decrease in voltage is consistent with TM reduction via oxygen loss[12] we acknowledge that there are many other possible contributors including intra-particle Li^+ homogenization, inter-particle Li^+ homogenization[47], self-discharge, and structure rearrangement[6,48] (e.g.TM migration[36]).

Discussion

We reveal that LMR-NMC loses oxygen at moderate SoCs during the first cycle, with irreversible oxygen loss occurring at SoCs as small as 135 mAh g^{-1}. The quantity of oxygen loss is also significant, as much as 2.7 at. % of oxygen after resting 100 h at 265 mAh g^{-1} (see Supplementary Table 2), corresponding to more than 7 mL of O_2 (25 ºC and 1 atm) loss per gram of LMR–NMC. While it oxygen loss is typically observed only at the end of charging[2,3,4,20,21], our findings paint a different picture in which oxygen is unstable throughout much of the charge/discharge cycle. Thermodynamically, our observations are consistent with the work from

Godshall et al., in which they correlated the equilibrium oxygen activity (aO_2) of ternary lithium transition metal oxide electrodes with the voltage obtained vs. a Li/Li^+ counter electrode[22]. They showed that for the specific case of an equilibrium between lithium oxide and two binary transition metal oxides (e.g. Li_2O, MO, and MO_2, in which M represents a single transition metal), the relationship between aO_2 and voltage at 25 ºC is described by:

$$E = 0.01476\ \log_{10}(aO_2) + 2.91\ V \qquad (3)$$

Employing this equation results in an equilibrium aO_2 of 10^{50} atm at 3.65 V, a seemingly moderate voltage which is well-surpassed even by the electrode that is charged to just 50 mAh g^{-1}. Godshall et al. also experimentally determined aO_2 and voltage values for many equilibrium mixtures of three phases (referred to as "tie triangles") with various crystal structures and compositions. Even when the components of a given tie triangle did not meet the requirements to solve for Eq. (3) analytically, the experimental relationship between voltage and aO_2 was found to be in close agreement to Eq. (3). These results therefore imply that Eq. (3) combined with a voltage measurement is a reasonable estimator of the equilibrium aO_2 in layered oxide positive electrodes. In Supplementary Note 2, we additionally provide a defect chemical derivation to further support the instability of oxygen based on the DFT results in Fig. 4b (also see Supplementary Fig. 8).

In summary, the large aO_2 at moderate potential establishes the driving force for oxygen loss, while the low oxygen vacancy formation energy determines the equilibrium fraction of oxygen vacancies. We note that surface TM reduction has been found in electrodes which are soaked in electrolyte without even being charged[34], providing further experimental evidence that layered oxide materials are thermodynamically unstable to oxygen loss even at low SoCs (Supplementary Note 2)[34]. Furthermore, we emphasize that the formation of trapped dimerized O_2[6–10] is consistent with this picture, as it indicates a thermodynamic instability with respect to dimerized O_2 and an oxygen-deficient layered oxide[27].

Finally, the results shown in Fig. 1b imply that the oxygen loss process partially passivates over time. To demonstrate this, we approximate the process as diffusion-limited in which oxygen is mobile with a constant diffusivity when the SoC is over 135 mAh g^{-1}

(corresponding to a Li content of ~ 0.75) and has no mobility below this SoC (Supplementary Fig. 9a). Using this simple model (Supplementary Note 3, Supplementary Fig. 10), for each electrode that is charged beyond 135 mAh g^{-1} (Supplementary Table 2), we fit an effective oxygen diffusivity to account for the experimentally determined Mn oxidation state. Interestingly, Supplementary Fig. 9b shows that this fitted oxygen diffusivity is highest in electrodes which are rested for only 1 min, while the electrodes which experience 100 hr or 150 hr rests can be fitted with a lower oxygen diffusivity. This result implies that the oxygen diffusion and loss process is passivating over time. We believe that the most likely reason for the passivation of oxygen diffusion/loss is the formation and stabilization of a surface reconstruction layer[34,18], which may serve to block oxygen from leaving the primary particles.

Implications for Designing Lithium-ion Positive Electrodes

Our results have significant implications for strategies to prevent oxygen loss from LMR layered oxide electrodes over cycling. The large equilibrium oxygen activity, together with the predicted negative oxygen vacancy formation energy (Fig. 4b), establishes the thermodynamic favorability of oxygen vacancy formation at moderate SoCs. Experimentally, our results demonstrate that the thermodynamic instability[22,49] of oxygen can have severe consequences for LMR electrodes, even when avoiding aggressive cycling conditions. As such, thermodynamically stabilizing oxygen atoms in layered oxide electrodes will be challenging. Instead, inhibiting the kinetics of oxygen diffusion and loss offers a more viable approach to keep oxygen within the structure during cycling.

The importance of oxygen diffusion kinetics underscores the need to understand the factors which affect oxygen diffusivity within layered oxides. Efforts to establish the oxygen diffusion mechanism, which to date have included studies of O^- hopping[28], oxygen vacancy migration[11], and fluid O_2[27], are valuable. Likewise, direct comparison of oxygen loss in 'Li stoichiometric' layered oxides (i.e. $LiTMO_2$), in which each oxygen atom in the ideal lattice has three covalent TM–O bonds, and Li-rich compounds, where many oxygens will have only two covalent TM–O bonds[50], will prove insightful. The additional TM–O bonds in 'Li stoichiometric' oxides may prevent oxygen dimerization and kinetically mitigate oxygen loss, an explanation consistent with the fact that LMR materials with a lower Li:TM ratio at the surface

experience less oxygen loss over cycling[51]. Further studies should also be conducted on Na-ion materials which exhibit few TM–O bonding partners but virtually no first-cycle oxygen loss[52]. Conformal coatings, while they can be difficult to synthesize[53], may be an effective method of mitigating oxygen loss while being semi-permeable to Li. To this end, our results call for the tracking of TM oxidation states over time in coated materials to assess long-term oxygen impermeability. Finally, our results confirm that limiting the time spent at high SoCs should increase the voltage retention of layered oxide electrodes[54].

Conclusions

We utilize X-ray spectroscopy, microscopy, and diffraction to isolate the effect of Li content on irreversible oxygen loss in LMR-NMC electrodes during calendar aging. Our results reveal that oxygen is both thermodynamically unstable and partially mobile at moderate SoCs (e.g. ~ 135–200 mAh g^{-1}). While this finding may be surprising, it is consistent with the thermodynamic relationship between Li chemical potential (voltage) and oxygen activity in other Li-containing systems. Mechanistically, oxygen sites with more Li neighbors, which are created through cation disorder, are more energetically favorable in accommodating oxygen vacancies. Notably, our calculations indicate that cation disordering gives rise to oxygen sites with a negative oxygen vacancy formation energy, even at full lithiation. We further show that LMR-NMC exhibits a large chemical expansion coefficient with respect to oxygen nonstoichiometry, approximately three times larger than typical fluorite and perovskite oxides. This large chemical expansion, alongside lattice contraction during delithiation, will accelerate material degradation through cracking. Our findings emphasize the need to improve our understanding of oxygen transport through Li-ion layered oxide electrodes and highlight the importance of utilizing calendar aging experiments to assess electrode aging.

Acknowledgements

This work was supported by the Assistant Secretary for Energy Efficiency and Renewable Energy, Office of Vehicle Technologies, Battery Materials Research Program, US Department of Energy (DOE). M.S.I. and K.M. are grateful to the Faraday Institution CATMAT project (EP/S003053/1, FIRG016) for financial support, and to the HEC Materials Chemistry Consortium (EP/R029431/1) for Archer-2 supercomputer facilities. P.M.C. acknowledges

support through the Stanford Graduate Fellowship as a Winston and Fu-Mei Chen fellow and through the National Science Foundation Graduate Research Fellowship under Grant no. DGE-1656518. D.F.R. acknowledges support through the National Science Foundation Graduate Research Fellowship under Grant no. DGE-2146755. Use of the SSRL, SLAC National Accelerator Laboratory, is supported by the U.S. Department of Energy, Office of Science, Office of Basic Energy Sciences under Contract No. DE-AC02-76SF00515. This research used resources of the Advanced Light Source, which is a DOE Office of Science User Facility under contract no. DE-AC02-05CH11231. We thank Samsung Advanced Institute of Technology (Sung-Jin Ahn) for providing the material used in this work.

Author Contributions

P.M.C. and W.C.C. conceived the study. P.M.C. performed electrochemical cycling experiments and cell disassembly. P.M.C., K.L., and G.M.B. collected TM K-edge spectra and analyzed the data. P.M.C. and D.A.S. collected and analyzed the STXM data. P.M.C., K.L., and G.M.B. collected and analyzed X-ray diffraction data. K.M. and M.S.I. carried out the DFT calculations and analyzed the results. G.M.B, D.F.R. and W.C.C. developed the defect chemical model discussed in Supplementary Note 2. P.M.C., K.M., and W.C.C. wrote the manuscript and all the authors revised the manuscript.

Competing Interests

The authors declare no competing interests.

Data Availability

All data supporting the findings of this study are available on request, and a public repository will be made available before final publication in a peer-reviewed journal.

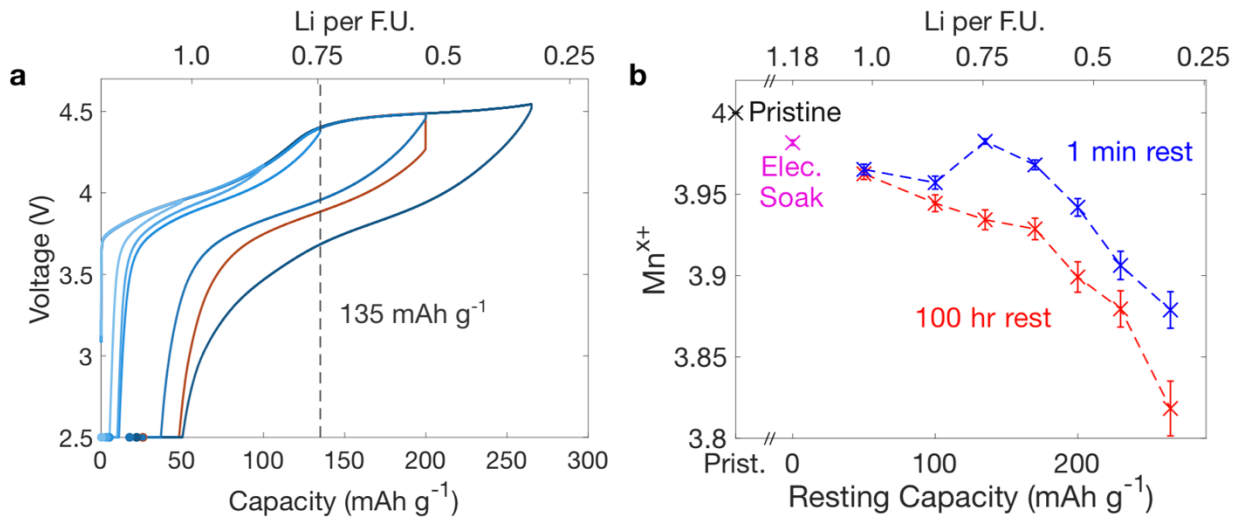

Figure 1. Transition metal reduction as a function of Li content. a Electrochemical cycling curves of pristine LMR-NMC being charged to various SoCs (13.5 mA g^{-1}) before being discharged (also see Supplementary Fig. 6). The high-voltage plateau begins after approximately 135 mAh g^{-1} of charge has passed. For the curves shown in blue, a 1 min OCV rest is performed in between charge and discharge. A 100 hr OCV rest is performed for the curve in red (also see Supplementary Fig. 6). The circular point for each curve represents the end of the constant voltage hold on discharge. **b** The Mn oxidation state as a function of electrochemical protocol. More Mn reduction occurs for cells which are charged to a higher capacity (lower Li content). More Mn reduction also occurs for cells which experience a 100 hr OCV rest period, particularly at higher SoCs. We note that a separate cell was tested for each ex situ data point used in this figure.

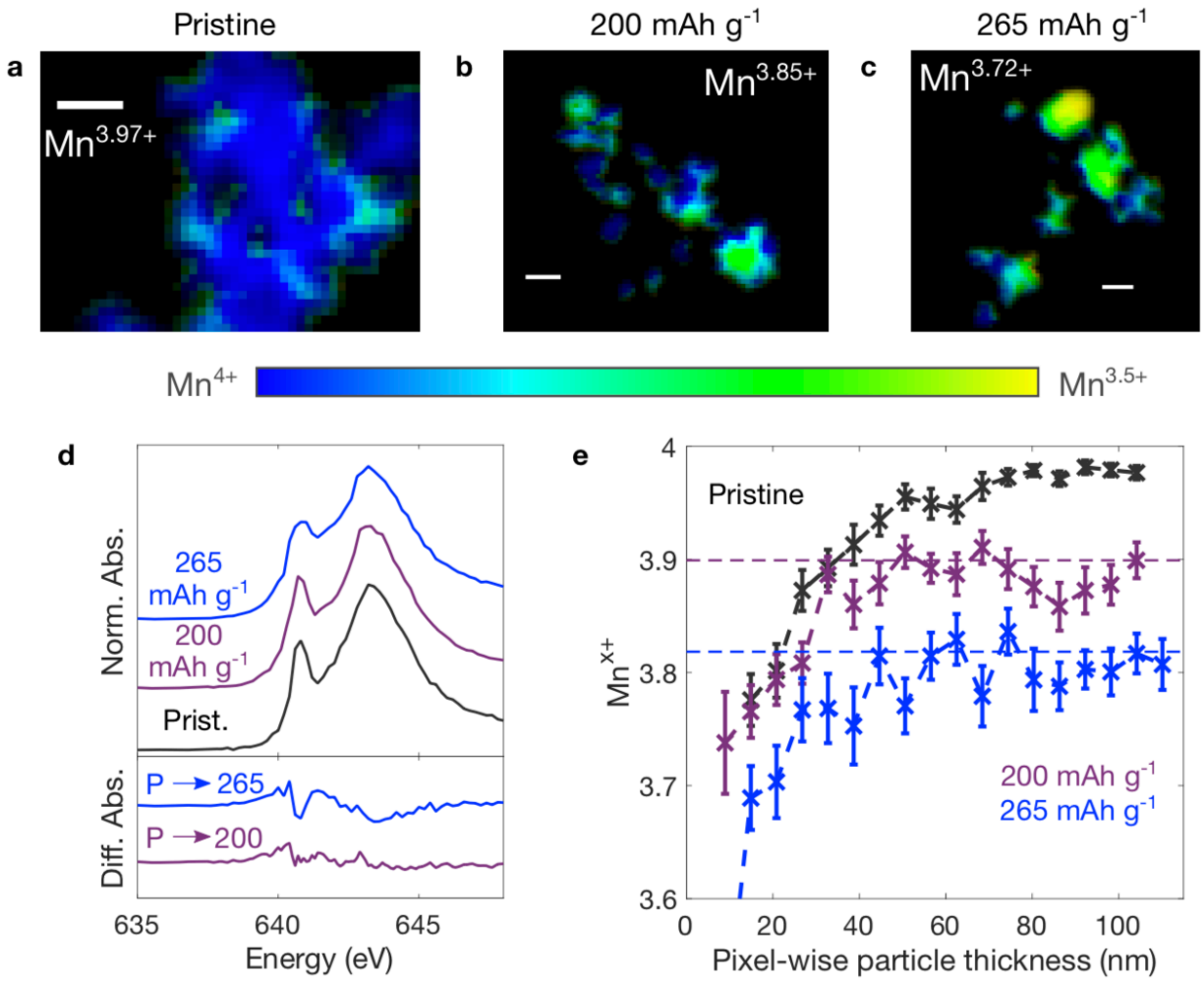

Figure 2. Spatial dependence of the Mn oxidation state. The electrodes shown are **a** the pristine material **b** an electrode charged to 200 mAh g^{-1} before being discharged and **c** an electrode charged to 265 mAh g^{-1} before being discharged. The electrodes in (b) and (c) both experienced a 100 hr open-circuit voltage resting period between charge and discharge. The scale bar in each image is 400 nm. **d** The bulk-averaged spectra showing that the electrodes which reach a higher capacity on charge exhibit a more reduced Mn oxidation state at the end of discharge (also see Supplementary Figure 11). **e** The Mn oxidation state determined by the fraction of the Mn^{3+} end member spectrum (see Supplementary Figure 11) found in each electrode as a function of the pixel-wise particle thickness (see Methods). The significant amount of Mn reduction even in thicker regions indicates that some amount of bulk reduction occurs within a single electrochemical cycle. The dotted lines correspond to the bulk-averaged oxidation states determined through Mn K-edge spectroscopy (Fig. 1b). Only data points resulting from the weighted average of over 10 pixels are included to avoid misinterpreting results originating from a small number of individual pixels.

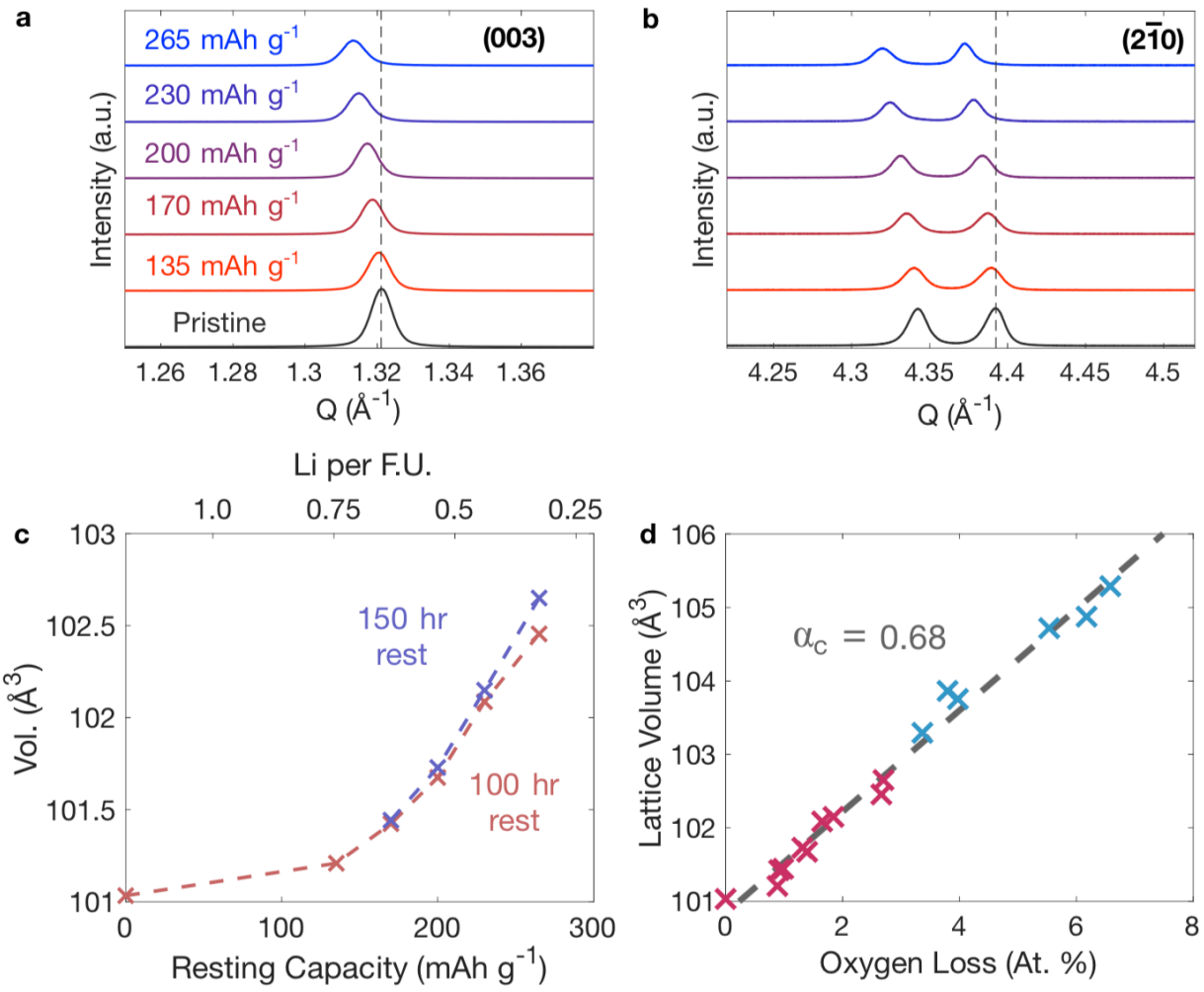

Figure 3. Lattice expansion as a function of the upper capacity cutoff. a The (003) peak and **b** the (2$\bar{1}$0) peak of the lithiated material indicate that the material remains in the original layered phase at the completion of the cycling protocol (see also Supplementary Fig. 1). For cells which experience a higher upper capacity cutoff, the two peaks shift to lower Q, indicating an expansion of the lattice (Supplementary Fig. 2). All electrodes shown here experienced a 100 hr open-circuit rest period. We note that the peak at lower Q (Q < 4.35 Å^{-1}) in panel b is the (10$\bar{8}$) peak. **c** The lattice volume increases with upper capacity cutoff, which we attribute to oxygen loss[11]. Longer rest times at the upper capacity cutoff result in more lattice expansion, although little difference is observed between electrodes which experience a 100 hr rest and those which experience a 150 hr rest. **d** The lattice volume is highly correlated with the amount of oxygen loss (see Supplementary Tables 2 and 3) for all electrodes measured, suggesting that the lattice volume in the fully discharged state can be used as an estimate for the amount of oxygen loss. Note that the six data points in blue are taken from a previous work[11] which examined the same material considered here after up to 500 electrochemical cycles. The pristine electrode with zero oxygen loss is also the same as in our previous work[11]. The Pearson's correlation coefficient for the data shown in this panel is 0.98. The data indicate a chemical expansion coefficient of α_c = 0.68 through the equation $\varepsilon = \alpha_c[V_O^{\cdot\cdot}]$.

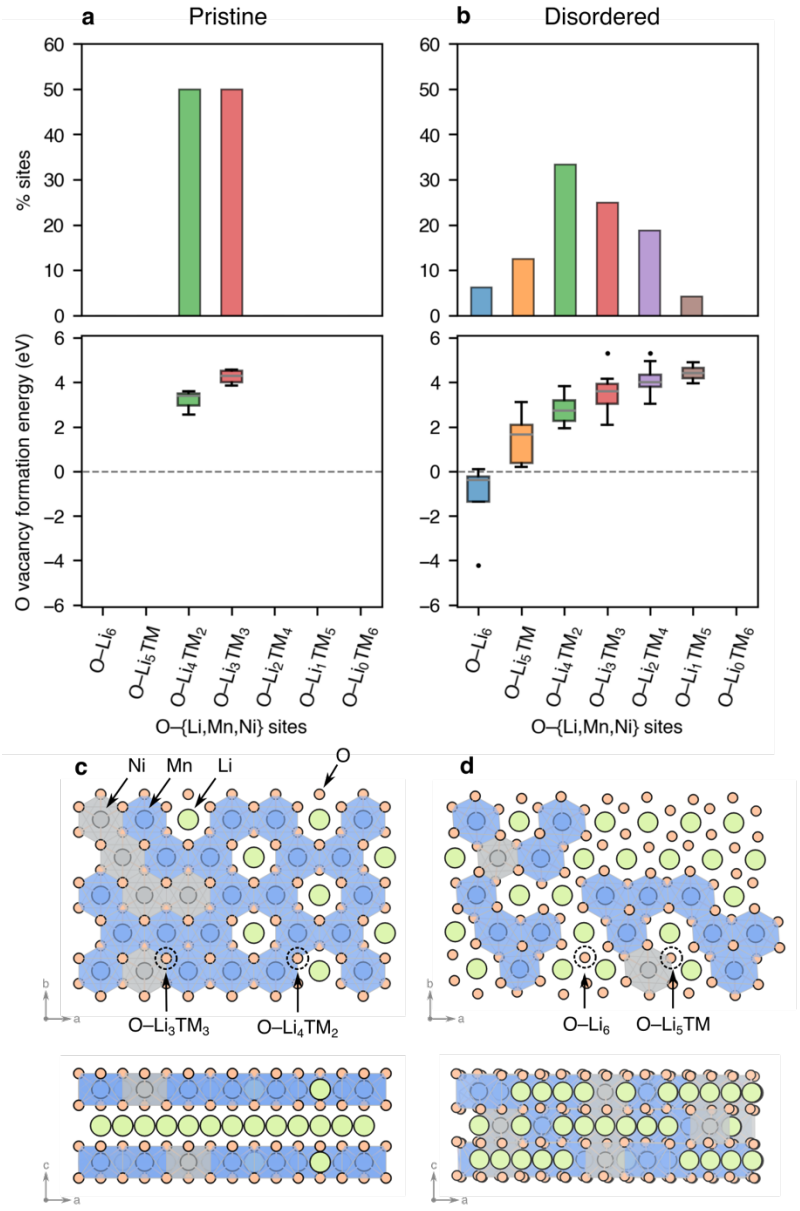

Figure 4. **Oxygen environments and oxygen vacancy formation energies. a** (top) Distribution of oxygen coordination environments in pristine $Li_{1.16}Mn_{0.67}Ni_{0.16}O_2$ obtained from the cluster expansion and Monte Carlo simulations; all sites are either O–Li_3TM_3 or O–Li_4TM_2. (bottom) Formation energy of oxygen vacancies $\Delta E(O_{vac})$, as a function of oxygen coordination environment for six sites in the pristine structure **b** (top) Distribution of oxygen coordination environments in a special quasirandom structure (SQS) model, representing configurational site disorder in the cycled electrode. The SQS model contains new O–Li_6, O–Li_5TM, O–Li_2TM_4 and O–$LiTM_5$ environments. (bottom) Oxygen vacancy formation energies of 48 O sites in the SQS structure. **c** Structure of pristine material (top and side view). **d** Structure of cycled material (top and side view).

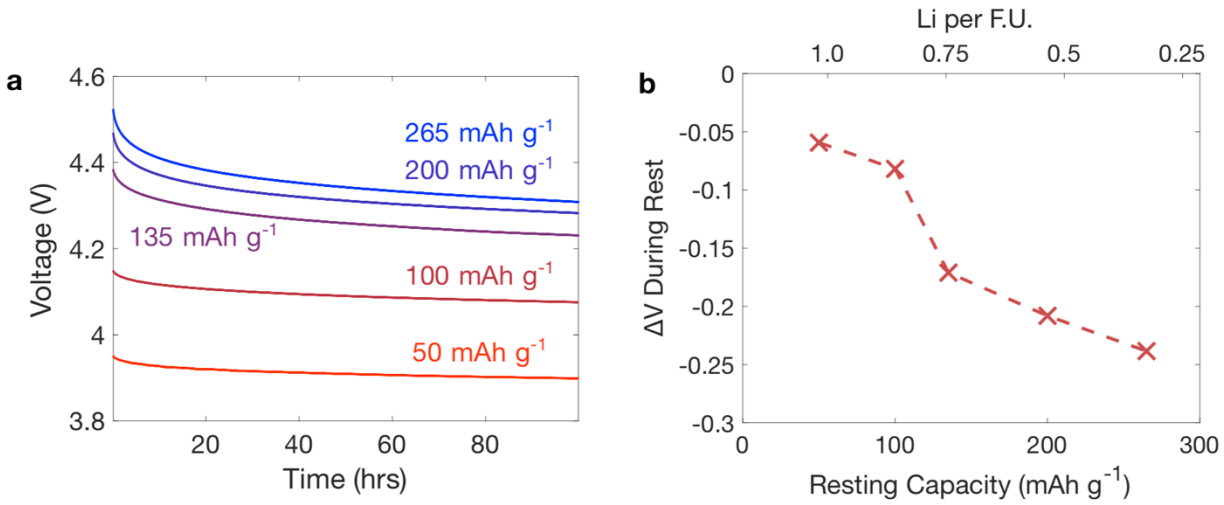

Figure 5. Voltage drop during open-circuit relaxation. a The voltage decay during a 100 hr open-circuit relaxation for cells which were first charged to different SoCs. **b** The change in open-circuit voltage during relaxation as a function of the resting capacity achieved on charge. We believe that this cannot be explained from the small amount of self-discharge which may occur during OCV resting (Supplementary Figure 7).

Methods:

Materials: $Li_{1.18}Mn_{0.53}Ni_{0.21}Co_{0.08}O_2$ was synthesized as previously reported[36]. Briefly, a mixed transition metal hydroxide precursor was coprecipitated from transition metal sulfate salts. The precursor was then mixed with Li_2CO_3 and calcined. This material stoichiometry was measured by ICP-MS, and was used for all calculations in the text.

Electrochemical Testing: Electrode sheets were fabricated with 80% active material, 10% carbon black, and 10% polyvinylidene fluoride (PVDF). We utilized a microbalance (XPR2, Mettler Toledo) to mass the electrodes. 2032-type coin cells were used for all electrochemical tests. The cells were fabricated in an argon filled glove box using metallic lithium counter electrodes. A EC:DEC (1:1 by weight) electrolyte with 1M $LiPF_6$ was utilized. A BCS-805 (Bio-logic) potentiostat was used for cycling. For the C/20 rate stated in the text, the rate that was used for all electrochemistry in this work, a theoretical capacity of 270 mAh g^{-1} was used.

Scanning transmission x-ray microscopy: Sonication and dispersion was used to prepare samples after removal from coin cells as reported previously[36]. The samples were sealed under argon and taken to the Advanced Light Source (ALS) at Lawrence Berkeley National Laboratory. A 45 nm zone plate was used, and a detailed description of the data analysis method can be found in our previous work[11]. We note that the sum of linear combination coefficients was used for determining the pixel-wise particle thickness (see Supplementary Figure 33 in our previous work[11]). The reference spectrum (see Supplementary Figure 11) for Mn_2O_3 was taken from previous work[11], while the reference spectrum for the pristine sample was taken from the sample shown in Fig. 2a in the main text.

X-ray diffraction: Synchrotron X-ray diffraction was performed and analyzed as described in our previous work[11]. Briefly, we utilized a 17 keV beam energy at beamline 2-1 at the Stanford Synchrotron Radiation Lightsource (SSRL). Note that the pristine sample XRD pattern is the same as was used previously[11].

X-ray absorption spectroscopy: X-ray absorption was conducted following the method described in our previous work[11]. Briefly, X-ray absorption was conducted at beamline 2-2 at SSRL in transmission mode. The electrodes harvested from cells were sealed under a pouch under argon. The data was analyzed using the ATHENA software package[55]. We note that the pristine sample XAS data was also used in previous work[11].

DFT Calculations: To determine the structure of pristine (uncycled) electrode and the frequency of different oxygen environments present, we fitted a cluster expansion model to $Li_{1.16}Mn_{0.67}Ni_{0.16}O_2$, using the *ICET* code, and ran Metropolis-Hastings lattice Monte Carlo simulations using the *mchammer* module of *ICET*[56]. To fit the CE, we used a ternary Li-Mn-Ni basis, in the primitive rocksalt unit cell, using structures based upon *R-3m* conventional unit cell of layered O3–$LiCoO_2$. The fit consisted of pair interactions up to 7.5 Å, triplet interactions up to 4.5 Å, and quadruplet interactions up to 4.5 Å. The cluster expansion was fitted with structures and energies from 190 density functional theory (DFT) calculations at the PBE+U level of theory in structures formed from (2×2×1) and (3×2×1) expansions of the conventional $LiCoO_2$ unit cell.

Relaxed structures from the DFT calculations were mapped back onto the primitive unit cell lattice using the *map_structure_to_reference* tool in ICET.

An initial set of 50 training structures was generated at random. From this training set, a low-quality cluster- expansion fit was obtained. Using this CE Hamiltonian, we ran lattice Monte Carlo simulations at temperatures between 0K and 1000K to generate additional structures with which to re-train the CE, and this procedure was repeated several times The cluster expansion was fitted with a k-fold cross-validation, scheme, using a set of 10 splits. The effective cluster interactions (ECIs) were obtained using a least absolute shrinkage and selection operator (LASSO) regression analysis, with a recursive feature elimination (RFE) approach, in which minimally contributing parameters are removed recursively, and the cross-validation score calculated, repeated until the cross-validation score no longer improves. The LASSO + RFE approach resulted in a fit with 25 non-zero ECIs. The final CE was fitted with a k-fold cross-validation root-mean-squared error (RMSE) obtained by the LASSO + RFE approach of 6 meV atom^{-1}.

To obtain structures to sample different local oxygen-ion environments, we generated a structure of layered LNMO in a 24×24×3 expansion of the conventional *R-3m* unit cell (containing 6912 atoms) with a random distribution of Li, Ni and Mn in the transition metal layers, and ran Monte Carlo simulations of the cell at a constant temperature of 1173 K, which is the calcination temperature previously used to produce LMR-NMC[11]. The Monte Carlo simulations were run for 1,000,000 MC cycles, and from the second half of this trajectory, we sampled 1000 structures to analyze their local environments. Analysis of the local environments used the Python *polyhedral_analysis* code[57]. To obtain a structure with local environments representing those in the cycled electrode, we generated a special quasirandom structure (SQS) model using the ICET code, which implements the algorithm proposed by Zunger et al.[44]

First-principles density functional theory (DFT) geometry relaxations, using the DFT+*U* approach, were performed to generate a training set of structures to parameterize the cluster-expansion model. All DFT+*U* calculations were performed using the plane-wave DFT Vienna Ab Initio Simulation Package (VASP) code[58–60]. Valence electrons were described by a plane-wave basis set with a cutoff of 550 eV. Interactions between core and valence electrons were described using the projector-augmented wave (PAW) method. Electronic exchange and correlation were approximated using the semi-local Perdew–Burke–Ernzerhof (PBE) generalized gradient approximation (GGA) functional, with a rotationally averaged Hubbard *U* correction[61] of 3.9 eV applied to the Mn 3d orbitals, and 6.2 eV to the Ni 3d orbitals to correct the self-interaction error (SIE)[62]. Reciprocal space was sampled with a discretization of 25 k-points Å^{-1}, and the electronic and ionic loops were converged with tolerances of 10^{-6} eV and 0.02 eV Å^{-1} for the total energy and interatomic forces respectively. All calculations were initialized with transition metal ions in a ferromagnetic configuration. Dispersion forces were included using Grimme's semiclassical D3 correction[63].

To calculate accurate oxygen vacancy formation energies, we used hybrid-exchange DFT calculations in the local basis set CRYSTAL17 code[64]. Oxygen vacancy calculations were performed on a layered structural models in a 4×3×1) expansion of the conventional unit cell, containing 144 atoms, and a SQS cell containing 92 atoms. Oxygen atoms were systematically removed from the structure, which was then fully-relaxed. Electronic exchange and correlation

were approximated using the screened hybrid-exchange functional HSE06[65]. Dispersion forces included using Grimme's semiclassical D3 correction[63]. All-electron atom-centered Gaussian basis sets were used for all atoms, available from the CRYSTAL online database (www.crystal.unito.it), with the online labels: Li (Li_511(1d)G_baranek_2013_LiNbO3), Mn (Mn_86-411d41G_towler_1992), Ni (Ni_86-411(41d)G_towler_1992) and O (O_8-411d1_cora_2005). The Coulomb and exchange series were truncated with thresholds of 10^{-7}, 10^{-7}, 10^{-7}, 10^{-7} and 10^{-14}, as described in the CRYSTAL manual. Reciprocal space was sampled using 3×3×3 Pack-Monkhorst grid for the 144 atom (4×3×1) unit cell and a 4×4×4 mesh for the SQS cell[66]. The self-consistent field (SCF) procedure was performed up to a convergence threshold of $\Delta E = 10^{-7}$ Hartree per unit cell. Calculations were initialized with all transition metal ions a ferromagnetic ordering and converged in the absence of spin constraints. All structures were full relaxed (lattice parameters and atomic positions) in the absence of symmetry, using the default force and energy convergence criteria in CRYSTAL17. Such a computational approach has been applied to recent studies of Li-rich electrode[6–8].

References:

1. Sharifi-Asl, S., Lu, J., Amine, K. & Shahbazian-Yassar, R. Oxygen Release Degradation in Li-Ion Battery Cathode Materials: Mechanisms and Mitigating Approaches. *Adv. Energy Mater.* **9**, 1–19 (2019).

2. Strehle, B. *et al.* The Role of Oxygen Release from Li- and Mn-Rich Layered Oxides during the First Cycles Investigated by On-Line Electrochemical Mass Spectrometry. *J. Electrochem. Soc.* **164**, A400–A406 (2017).

3. Teufl, T., Strehle, B., Müller, P., Gasteiger, H. A. & Mendez, M. A. Oxygen Release and Surface Degradation of Li- and Mn-Rich Layered Oxides in Variation of the Li2MnO3 Content. *J. Electrochem. Soc.* **165**, A2718–A2731 (2018).

4. Luo, K. *et al.* Charge-compensation in 3d-transition-metal-oxide intercalation cathodes through the generation of localized electron holes on oxygen. *Nat. Chem.* **8**, 684–691 (2016).

5. Sun, J. *et al.* Restraining Oxygen Release and Suppressing Structure Distortion in Single-Crystal Li-Rich Layered Cathode Materials. *Adv. Funct. Mater.* **32**, 1–7 (2022).

6. House, R. A. *et al.* Delocalized electron holes on oxygen in a battery cathode. *Nat. Energy* **8**, (2023).

7. McColl, K. *et al.* Transition metal migration and O2 formation underpin voltage hysteresis in oxygen-redox disordered rocksalt cathodes. *Nat. Commun.* **13**, 1–8 (2022).

8. Sharpe, R. *et al.* Redox Chemistry and the Role of Trapped Molecular O2in Li-Rich Disordered Rocksalt Oxyfluoride Cathodes. *J. Am. Chem. Soc.* **142**, 21799–21809 (2020).

9. House, R. A. *et al.* Superstructure control of first-cycle voltage hysteresis in oxygen-redox cathodes. *Nature* **577**, 502–508 (2019).

10. House, R. A. *et al.* First-cycle voltage hysteresis in Li-rich 3d cathodes associated with molecular O2 trapped in the bulk. *Nat. Energy* **5**, 777–785 (2020).

11. Csernica, P. M. *et al.* Persistent and partially mobile oxygen vacancies in Li-rich layered oxides. *Nat. Energy* **6**, 642–652 (2021).

12. Hu, E. *et al.* Evolution of redox couples in Li- and Mn-rich cathode materials and mitigation of voltage fade by reducing oxygen release. *Nat. Energy* **3**, 690–698 (2018).

13. Yang, F. *et al.* Nanoscale morphological and chemical changes of high voltage lithium-manganese rich NMC composite cathodes with cycling. *Nano Lett.* **14**, 4334–4341 (2014).

14. Yan, P. *et al.* Injection of oxygen vacancies in the bulk lattice of layered cathodes. *Nat.*

Nanotechnol. **14**, 602–608 (2019).

15. Zheng, J. *et al.* Structural and Chemical Evolution of Li- and Mn-Rich Layered Cathode Material. *Chem. Mater.* **27**, 1381–1390 (2015).

16. Mohanty, D. *et al.* Correlating cation ordering and voltage fade in a lithium-manganese-rich lithium-ion battery cathode oxide: A joint magnetic susceptibility and TEM study. *Phys. Chem. Chem. Phys.* **15**, 19496–19509 (2013).

17. Qian, D., Xu, B., Chi, M. & Meng, Y. S. Uncovering the roles of oxygen vacancies in cation migration in lithium excess layered oxides. *Phys. Chem. Chem. Phys.* **16**, 14665–14668 (2014).

18. Boulineau, A., Simonin, L., Colin, J. F., Bourbon, C. & Patoux, S. First evidence of manganese-nickel segregation and densification upon cycling in Li-rich layered oxides for lithium batteries. *Nano Lett.* **13**, 3857–3863 (2013).

19. Wen, B. *et al.* Surface reduction in lithium- and manganese-rich layered cathodes for lithium ion batteries drives voltage decay. *J. Mater. Chem. A* **10**, 21941–21954 (2022).

20. Renfrew, S. E. & McCloskey, B. D. Residual Lithium Carbonate Predominantly Accounts for First Cycle CO2and CO Outgassing of Li-Stoichiometric and Li-Rich Layered Transition-Metal Oxides. *J. Am. Chem. Soc.* **139**, 17853–17860 (2017).

21. Xu, J. *et al.* Elucidating anionic oxygen activity in lithium-rich layered oxides Jing. *Nat. Commun.* **9**, 947

22. Godshall, N. A., Raistrick, I. D. & Huggins, R. A. Relationships among Electrochemical, Thermodynamic, and Oxygen Potential Quantities in Lithium-Transition Metal-Oxygen Molten Salt Cells. *J. Electrochem. Soc.* **131**, 543–549 (1984).

23. Huggins, R. A. *Advanced batteries: Materials science aspects*. *Advanced Batteries: Materials Science Aspects* (2009). doi:10.1007/978-0-387-76424-5

24. Bak, S. M. *et al.* Structural changes and thermal stability of charged LiNixMnyCozO2 cathode materials studied by combined in situ time-resolved XRD and mass spectroscopy. *ACS Appl. Mater. Interfaces* **6**, 22594–22601 (2014).

25. Nakamura, T. *et al.* Impact of oxygen defects on electrochemical processes and charge compensation of Li-rich cathode material Li1.2Mn0.6Ni0.2O2−δ. *ACS Appl. Energy Mater.* **3**, 9703–9713 (2020).

26. Nakamura, T. *et al.* Defect chemical studies on oxygen release of Li-rich cathode material Li1.2Ni0.2Mn0.6O2-d. *J. Mater. Chem. A* (2019). doi:10.1039/C8TA12484A

27. McColl, K., Coles, S. W., Zarabadi-poor, P., Morgan, B. J. & Islam, M. S. Phase

segregation and nanoconfined fluid O2 in a lithium-rich oxide cathode. *ChemRxiv* 1–12 (2023). doi:10.26434/chemrxiv-2023-9v2dw

28. Lee, E. & Persson, K. A. Structural and Chemical Evolution of the Layered Li-Excess LixMnO3 as a Function of Li Content from First-Principles Calculations. *Adv. Energy Mater.* **4**, 1400498 (2014).

29. Gerbig, O., Merkle, R. & Maier, J. Electrical transport and oxygen exchange in the superoxides of potassium, rubidium, and cesium. *Adv. Funct. Mater.* **25**, 2552–2563 (2015).

30. Gent, W. E., Abate, I. I., Yang, W., Nazar, L. F. & Chueh, W. C. Design Rules for High-Valent Redox in Intercalation Electrodes. *Joule* **4**, 1369–1397 (2020).

31. Hong, J. *et al.* Metal–oxygen decoordination stabilizes anion redox in Li-rich oxides. *Nat. Mater.* **18**, 256–265 (2019).

32. Sathiya, M. *et al.* Origin of voltage decay in high-capacity layered oxide electrodes. *Nat. Mater.* **14**, 230–238 (2015).

33. Sood, A. *et al.* Electrochemical ion insertion from the atomic to the device scale. *Nat. Rev. Mater.* **6**, 847–867 (2021).

34. Lin, F. *et al.* Surface reconstruction and chemical evolution of stoichiometric layered cathode materials for lithium-ion batteries. *Nat. Commun.* **5**, 3529 (2014).

35. Dau, H., Liebisch, P. & Haumann, M. X-ray absorption spectroscopy to analyze nuclear geometry and electronic structure of biological metal centers-potential and questions examined with special focus on the tetra-nuclear manganese complex of oxygenic photosynthesis. *Anal. Bioanal. Chem.* **376**, 562–583 (2003).

36. Gent, W. E. *et al.* Coupling between oxygen redox and cation migration explains unusual electrochemistry in lithium-rich layered oxides. *Nat. Commun.* **8**, 2091 (2017).

37. Bluhm, H. *et al.* Soft X-ray microscopy and spectroscopy at the molecular environmental science beamline at the Advanced Light Source. *J. Electron Spectros. Relat. Phenomena* **150**, 86–104 (2006).

38. Strehle, B. *et al.* Correlating the Voltage Hysteresis in Li- and Mn-Rich Layered Oxides to Reversible Structural Changes by Using X-ray and Neutron Powder Diffraction. *J. Electrochem. Soc.* **169**, 020554 (2022).

39. Marrocchelli, D., Bishop, S. R., Tuller, H. L. & Yildiz, B. Understanding chemical expansion in non-stoichiometric oxides: Ceria and zirconia case studies. *Adv. Funct. Mater.* **22**, 1958–1965 (2012).

40. Armstrong, T. R., Stevenson, J. W., Pederson, L. R. & Raney, P. E. Dimensional Instability of Doped Lanthanum Chromite. *J. Electrochem. Soc.* **143**, 2919–2925 (1996).

41. Kharton, V. V., Yaremchenko, A. A., Patrakeev, M. V., Naumovich, E. N. & Marques, F. M. B. Thermal and chemical induced expansion of La0.3Sr0.7 (Fe,Ga)O3-δ ceramics. *J. Eur. Ceram. Soc.* **23**, 1417–1426 (2003).

42. Bishop, S. R. *et al.* Chemical expansion: Implications for electrochemical energy storage and conversion devices. *Annu. Rev. Mater. Res.* **44**, 205–239 (2014).

43. Ceder, G. *et al.* High-resolution X-ray diffraction, DIFFaX, NMR and first principles study of disorder in the Li2MnO3–Li[Ni1/2Mn1/2]O2 solid solution. *J. Solid State Chem.* **178**, 2575–2585 (2005).

44. Zunger, A., Wei, S.-H., Ferreira, L. G. & Bernard, J. E. Special quasirandom structures. *Phys. Rev. Lett.* **65**, 353–356 (1990).

45. Sarkar, T., Prakasha, K. R., Bharadwaj, M. D. & Prakash, A. S. Li-Removal Mechanism and Its Effect on Oxygen Stability Influencing the Electrochemical Performance of Li1.17Ni0.17Mn0.67O2: Experimental and First-Principles Analysis. *J. Phys. Chem. C* **121**, 20591–20596 (2017).

46. Singer, A. *et al.* Nucleation of dislocations and their dynamics in layered oxide cathode materials during battery charging. *Nat. Energy* **3**, 641–647 (2018).

47. Park, J. *et al.* Fictitious phase separation in Li layered oxides driven by electro-autocatalysis. *Nat. Mater.* **20**, 991–999 (2021).

48. Li, B. *et al.* Decoupling the roles of Ni and Co in anionic redox activity of Li-rich NMC cathodes. *Nat. Mater.* (2023). doi:10.1038/s41563-023-01679-x

49. Huggins, R. A. Do You Really Want an Unsafe Battery? *J. Electrochem. Soc.* **160**, A3001–A3005 (2013).

50. Seo, D. *et al.* The structural and chemical origin of the oxygen redox activity in layered and cation-disordered Li-excess cathode materials. *Nat. Chem.* **8**, 692–697 (2016).

51. Zhu, Z. *et al.* Gradient Li-rich oxide cathode particles immunized against oxygen release by a molten salt treatment. *Nat. Energy* **4**, 1049–1058 (2019).

52. Maitra, U. *et al.* Oxygen redox chemistry without excess alkali-metal ions in Na2/3[Mg0.28Mn0.72]O2. *Nat. Chem.* **10**, 288–295 (2018).

53. Kim, S. Y. *et al.* Inhibiting Oxygen Release from Li-rich, Mn-rich Layered Oxides at the Surface with a Solution Processable Oxygen Scavenger Polymer. *Adv. Energy Mater.* **11**, 1–12 (2021).

54. Assat, G. *et al.* Fundamental interplay between anionic/cationic redox governing the kinetics and thermodynamics of lithium-rich cathodes. *Nat. Commun.* **8**, (2017).

55. Ravel, B. & Newville, M. ATHENA, ARTEMIS, HEPHAESTUS: Data analysis for X-ray absorption spectroscopy using IFEFFIT. *J. Synchrotron Radiat.* **12**, 537–541 (2005).

56. Ångqvist, M., Lindroth, D. O. & Erhart, P. Optimization of the Thermoelectric Power Factor: Coupling between Chemical Order and Transport Properties. *Chem. Mater.* **28**, 6877–6885 (2016).

57. Morgan, B. Polyhedral-Analysis. (2020). Available at: https://github.com/bjmorgan/polyhedral-analysis.

58. Kresse, G. & Hafner, J. Ab initio molecular dynamics for liquid metals. *Phys. Rev. B* **47**, 558–561 (1993).

59. Kresse, G. & Furthmüller, J. Efficiency of ab-initio total energy calculations for metals and semiconductors using a plane-wave basis set. *Comput. Mater. Sci.* **6**, 15–50 (1996).

60. Kresse, G. & Furthmüller, J. Efficient iterative schemes for ab initio total-energy calculations using a plane-wave basis set. *Phys. Rev. B - Condens. Matter Mater. Phys.* **54**, 11169–11186 (1996).

61. Dudarev, S. & Botton, G. Electron-energy-loss spectra and the structural stability of nickel oxide: An LSDA+U study. *Phys. Rev. B - Condens. Matter Mater. Phys.* **57**, 1505–1509 (1998).

62. Wang, L., Maxisch, T. & Ceder, G. Oxidation energies of transition metal oxides within the GGA+U framework. *Phys. Rev. B - Condens. Matter Mater. Phys.* **73**, 1–6 (2006).

63. Grimme, S., Antony, J., Ehrlich, S. & Krieg, H. A consistent and accurate ab initio parametrization of density functional dispersion correction (DFT-D) for the 94 elements H-Pu. *J. Chem. Phys.* **132**, (2010).

64. Dovesi, R. *et al.* Quantum-mechanical condensed matter simulations with CRYSTAL. *Wiley Interdiscip. Rev. Comput. Mol. Sci.* **8**, 1–36 (2018).

65. Heyd, J., Scuseria, G. E. & Ernzerhof, M. Hybrid functionals based on a screened Coulomb potential. *J. Chem. Phys.* **118**, 8207–8215 (2003).

66. Monkhorst, H. J. & Pack, J. D. Special points for Brillouin-zone integrations. *Phys. Rev. B* **13**, 5188–5192 (1976).